Article

Exchanging Anion in CuCo—Carbonate Double Hydroxide for Faradaic Supercapacitors: A Case Study

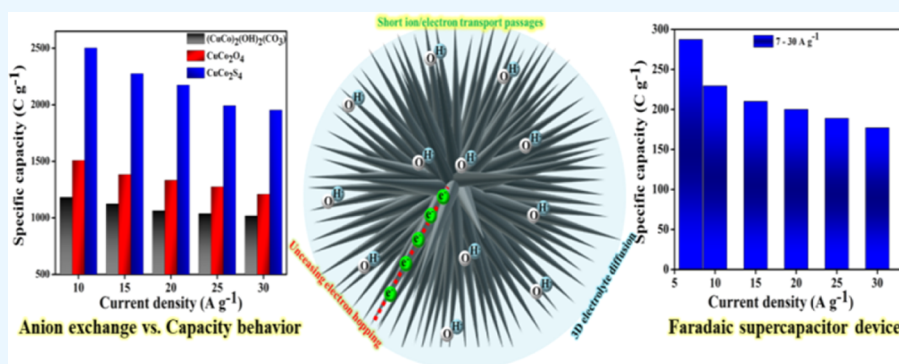Amala George and Manab Kundu*

Read Online

ACCESS | Metrics & More | Article Recommendations | Supporting Information

ABSTRACT: A systematic synthetic method involving the anion exchange process was designed and developed to fabricate the superior functioning three-dimensional (3-D) urchin-architectured copper cobalt oxide ($CuCo_2O_4$; CCO) and copper cobalt sulfide ($CuCo_2S_4$; CCS) electrode materials from copper−cobalt carbonate double hydroxide [$(CuCo)_2(CO_3)(OH)_2$; CCH]. The effective tuning of chemical, crystalline, and morphological properties was achieved during the derivatization process of CCH, based on the anion exchange effect and phase transformation without altering the 3-D spatial assembly. Benefiting from morphological and structural advantages, CCO and CCS exhibited superior electrochemical activity with capacity values of 1508 and 2502 C g^{-1} at 10 A g^{-1} to CCH (1182 C g^{-1} at 10 A g^{-1}). The thermal treatment of CCH has generated a highly porous nature in nanospikes of 3-D urchin CCO structures, which purveys betterment in electrochemical phenomena than pristine smooth-surfaced CCH. Meanwhile, the sulfurization reaction induced the anion effect to a greater extent in the CCS morphology, resulting in hierarchical 3-D urchins formed by 1-D nanospikes constituting coaxially swirled 2-D nanosheets with high exposure of active sites, specific surface areas, and 3-D electron/ion transportation channels. The asymmetric supercapacitor was constructed with a superior CCS electrode as a cathode and an activated carbon electrode as an anode, showing a high specific capacity of 287.35 C g^{-1} at 7 A g^{-1} and durability for 5000 cycles with 94.2% retention at a high current density of 30 A g^{-1}. The ultrahigh energy and power density of 135.3 W h kg^{-1} (10 A g^{-1}) and 44.35 kW kg^{-1} (30 A g^{-1}) were harvested during the PC device performance. Our finding proposes an idea about the importance of anions and phase transformation as a versatile tool for engineering high-functioning electrode materials and their endeavor toward overwhelming the major demerit of SCs by aggrandizing the energy density value and rate performance.

■ INTRODUCTION

The world is facing a major interconnected issue: energy crisis and environmental pollution. Urbanization, pollution, population, fossil fuel depletion, and climate change urge sustainable energy systems to develop carbon-neutral civilizations. Modern electric transportations and digital communications also require the development of energy storage units, which are safe, environmentally benign, low cost, durable, and perform with high power and energy density.[1] Among the various energy storage devices, electrochemical capacitors [also known as supercapacitors (SCs)] stand under the limelight, due to their cleaner, safer operations, high power density, prolonged durability, and rapid charging than commercial secondary batteries. However, the existing lower energy density of SCs (<10 W h kg^{-1}) compared to commercial Li-ion batteries (∼180

W h kg^{-1}) pulls the trends down commercially and invokes the need for development toward their improved and efficient performance.[2]

The major issues of the SCs are related to flaws in their electrode materials, which prevent/hamper the electrochemical reactions.[3] The design and fabrication of electrode materials with superior redox properties and conducting nature can

improvise the efficacy of SCs, over traditional physical adsorption−desorption-based carbonaceous electrode materials used in conventional electric double-layer capacitors (EDLCs).[4] In recent years, there have been numerous reports on the utilization of transition-metal derivatives as electrode materials in SCs with improved energy density, major functions depend on their redox nature and electron/ion transport capability, categorized as Faradaic capacitors (FCs) or pseudocapacitors (PCs).[5−7] In this case to tune the electrochemical and conductance characteristics, feasible electronic structures with impeccable morphological features and elemental compositions of electrode materials need to be optimized.[8−11]

Metal hydroxide (MHs)-based materials are reported as propitious electrodes for PCs with the advantages of high surface area, active site, shorter diffusion length, multi-redox states with tunable cation host layers, and predominant ion exchange capability.[12−14] Xu et al., reported $Cu(OH)_2$ electrode-based SCs providing 511.5 F g^{-1} capacitance value at a current density of 5 mA cm^{-2}.[15] As a well-established fact, ternary metal-based materials possess superior electrochemical properties than binary systems, due to their multivalence states, charge hopping, and improved electronic structure and conductivity.[16] 2-D copper cobalt double hydroxide materials were established by Deshmukh et al., providing 1032 F cm^3 at 10 mA cm^2 and the respective asymmetric device yielded a high energy density of 21.9 mW h cm^{-3}.[17]

In the MH family, similar to traditional layered double hydroxides (LDH), carbonate double hydroxide (CDH) has a general formula of $M_2CO_3(OH)_2$, constituting divalent metal host cation connected with hydroxyl anions and intercalated carbonate anions in the lattice structure.[18,19] The CDH are distinguished from conventional lamellar-structured LDH by the nonappearance of X-ray diffraction planes (003) and (006).[20] In CDH, along with the influences of metal compositions in host layers, the anion also has a great impact on electrochemical activity, as anion exchanging ease flawless ion transport throughout the material and improved porous structure. The positively charged host and the interaction of anions with cations enable the adsorption of anion species, which improves the OH$^-$ ion adsorption from the KOH solution. In general, the ion exchange equilibrium of various anions is in the following order PO_4^{3-} > CO_3^{2-} > SO_4^{2-} > OH$^-$ > F$^-$ > Cl$^-$ > NO_2^- > NO_3^- > I$^-$ ≫ organic anion.[21] Ni−Co LDH incorporated with CO_3^{2-} anion-based electrode was developed by Zou et al., resulting in an exceptionally high capacitance of 2391 F g^{-1} at 2 mA cm^{-2}, highlighting the reservoir characteristic of CO_3^{2-} anions for OH$^-$ transportation as an effect of anion exchange between CO_3^{2-} and OH$^-$ anions from the electrolyte solution.[22] Hence, along with the metal cation alteration by tuning the anion also, the capacitive performance can be improved with better OH$^-$ ion exchange, accommodation, and transportation during the charge storage process. However, according to the intercalation thermodynamics, the possible affinity between CO_3^{2-} and host layer cations can cause a drastic drop in capacitive behavior by a decrement in OH$^-$ ion exchange.[23] Despite CDH having a good electrochemical nature, the poor electrical conductivity and structural instability hamper the cycling duration and rate performance. Thus, the conversion of CDH to their derivatives (oxides, sulfides, phosphides, selenides, and nitrides) aids to improve the electrical conductivity and preserves the morphological and chemical advantages of CDH, improving the electrochemical activity to a greater extent.[24−28]

The simplest route to enhance the electrical conductivity of CDH is converting to the respective oxide by heat treatment in the air atmosphere. The heat treatment causes a dehydration reaction and results in ternary metal oxide ($A_xB_yO_z$) formation with multiple oxidation and coordination states and chemical stability. Li et al. developed $NiCo_2O_4$/rGO composites from NiCo LDH viz exfoliation followed by annealing, created open electron channels through the dehydration reaction for rapid electron mobility. The respective $NiCo_2O_4$/rGO electrode provided a specific capacitance of 1338 F g^{-1} at 0.5 A g^{-1} with enhanced durability for 20,000 cycles at 5 A g^{-1} with a 90.2% retention value.[29] The electrochemical activity of oxide is interconnected with the interaction of OH$^-$ with metallic active sites, where the porous architecture enhances the contact, hopping, transportation, and storage, boosting the capacitive behavior.[30] Regardless of the advantages of oxide derivatives, $A_xB_yO_z$ supplies poor electrical conductivity and lowers the capacitances than their theoretical values upon the charge storage process, owing to the lower activation energy for electron transfer.[31]

Generally, the smaller band gap of metal sulfides ameliorates their electrical conductivity than respective hydroxides and oxides due to the larger covalency of S^{2-} than O^{2-} anions.[32] During the conversion of CDH to sulfide, there is a steep increment in the pore size and surface area after the inclusion of S^{2-} in the matrix. S^{2-} ions has a larger anion size than O^{2-}, develops the larger strain in the crystal structure, and leads to lattice disorders, defects, and distortions at the heterojunction phase boundaries.[33−35] Capacitive performances of $Ni_XZn_{1-X}OH$ and derivative (NiO−ZnO, $Ni_XZn_{1-X}S$) electrodes were analyzed by Wang et al., where the obtained porous $Ni_XZn_{1-X}S$ electrode showed an enhanced surface area of 148.4 m^2 g^{-1} and delivered high capacitance (1867 F g^{-1} at 1 A g^{-1}).[36]

In addition to chemical and structural merits, the PC's performance is highly harmonized with the morphology of the material with architectural advantages. In general, MHs are 2-D hexagonal nanosheets arranged as lamellar layered materials (LDH), referred to as planar structures. To address the demand of electrode material evolution, the 3-D material design and development is an appropriate method, which can increase the electron and mass transfer and accommodation. The spatial structure of the 3-D material is formed by the assembly of 2-D units interconnected to each other hierarchically in space imparting a 3-D spatial configuration, which offers magnified spatial utilization and specific surface area.[37,38]

In this work, 3-D urchin-architectured copper−cobalt CDH [$(CuCo)_2(OH)_2(CO_3)$—CCH] materials were prepared with smooth surfaced 2-D nanospikes arranged in a 3-D manner to form urchins in a spatial arrangement. The derivatization of CCH to oxide ($CuCo_2O_4$—CCO) and sulfide ($CuCo_2S_4$—CCS) was carried out by annealing and hydrothermal treatment, respectively, without altering the 3-D morphology. $CuCo_2S_4$ has several advantages including s-wave superconductivity, low resistivity (10^{-4} Ω), and also multivalence states (Co^{2+}, Co^{3+}, and Cu^{2+}), leading to better capacity and rate capability performance.[39] As discussed earlier, the porosity was created in CCO nanospikes during thermal conversion, whereas CCS spikes resulted in 3-D scaffolded sheets along the 2-D spikes axis. Guo et al. reported that the sulfurization reaction transforms the smooth surfaced hydroxides into rough and flaky natured sulfide due to the S^{2-} anion replacement in the crystal lattice resulting in a high energy density of 50.56 W h kg^{-1} at 4.6 kW kg^{-1} power density and energy density withstands 20.93 W h kg^{-1} even at a

high power density of 22.5 kW kg^{-1}.[40] Hence, the derivatization of 3-D urchin CCH was optimized in a systematic manner and obtained an efficient electrode material with improved chemical, morphological, and electrical properties. The three-electrode configuration was assembled to study the influence of fabricated electrodes toward the half-cell reaction of PCs with cyclic voltammetry (CV), galvanic charge−discharge (GCD), and electrochemical impedance spectroscopy (EIS) techniques. An asymmetric SC device (ASC) was fabricated using CCS as the cathode material to study and highlight the effect of CDH derived electrode materials in improved capacity and energy density of PCs at a high applied current density of 30 A g^{-1}.

■ EXPERIMENTAL SECTION

Materials. All the experiments were performed using below-mentioned chemicals without any further purification techniques: ammonium fluoride (NH$_4$F, 99.5%, SRL), copper nitrate trihydrate (Cu(NO$_3$)$_2$·3H$_2$O, 99.99%, Sigma-Aldrich), cobalt nitrate hexahydrate (Co(NO$_3$)$_2$·6H$_2$O, 99.99%, Sigma-Aldrich), sodium sulfide (Na$_2$S·9H$_2$O, 60%, SRL), and urea (CH$_4$N$_2$O, 99%, SRL). Ni foam was purchased from Labkart India Scientific Solutions.

Preparation. The Ni foam pre-treatment was accomplished with a 3 M HCl solution for 15 min viz sonication, water and acetone washed, and dried at 90 °C for 4 h. Cu(NO$_3$)$_2$·3H$_2$O (241 mg), Co(NO$_3$)$_2$·6H$_2$O (582 mg), CH$_4$N$_2$O (900 mg), and NH$_4$F (224 mg) were dissolved in 40 mL of deionized water by sonication for 30 min, followed by magnetic stirring of the solution for 1 h at standard room temperature. The resultant pink solution with pre-treated Ni foam (1 × 1 cm^2) was transferred to a 50 mL Teflon autoclave and heated to 100 °C for 24 h resulting in the formation of urchin-like (Cu-Co)$_2$(OH)$_2$(CO$_3$). Formation of CuCo$_2$O$_4$ was achieved by annealing the obtained material [(CuCo)$_2$(OH)$_2$(CO$_3$)] at 350 °C for 3 h at an air atmosphere. The sulfurization process was carried out through a hydrothermal anion exchange process with the CuCo$_2$O$_4$ material at 100 °C for 10 h with 1.41 g Na$_2$S·9H$_2$O, leads to CuCo$_2$S$_4$ formation.

Material Characterization. Using Bruker USA D8 Advances, the crystallographic studies were done. A brief study on morphological features was analyzed using high-resolution scanning electron microscopy (HRSEM) (Thermo Scientific Apreo S) and high-resolution transmission electron microscopy (HRTEM) (JEOL Japan, JEM-2100 Plus). The nitrogen adsorption−desorption isotherms were performed with a Quantachrome-ASiQwin (version 5.0) apparatus and the porosity measurement was evaluated by Brunauer−Emmett−Teller (BET) and Barret−Joyner−Halenda (BJH) methods. With the aid of X-ray photoelectron spectroscopy (XPS) (Thermo Fisher Scientific Nexsa base), the elemental composition and metallic states were confirmed and electrochemical characterizations were implemented with an OrigaLys eletro-flex electrochemical workstation.

Electrochemical Measurements. The electrochemical characteristics of prepared electrodes (CCH, CCO, and CCS) were evaluated by a three-electrode system at room temperature. The Ni foam substrate-based electrodes (CCH, CCO, and CCS), Pt wire, and Ag/AgCl were exploited as working, counter, and reference electrodes, respectively. The electrochemical testings comprising cyclic voltammetry (CV) (0 to 0.7 V vs Ag/AgCl), galvanic charge−-discharge (GCD) (0 to 0.6 V vs Ag/AgCl), and electrochemical impedance spectroscopy (EIS) (100 mHZ to 100 kHz at AC amplitude of 5 mA) were done in a 3 M

KOH electrolyte. The specific capacity values were calculated from GCD curves using following eq 1.[41]

$$Cs = \frac{I\Delta t}{m} \tag{1}$$

In the above equation, the I (A), Δt (s), and m (g) are the current applied, discharge time, and mass loading of samples.

The frequency-dependent capacitive behavior of the electrodes was estimated from EIS results using below eq 2

$$Cs = \frac{1}{2\pi f m Z''} \tag{2}$$

In eq 2, m (g), f (Hz), and Z'' are mass loading of samples, frequency, and imaginary parts from EIS data.

An ASC (Swagelok cell) was assembled with CCS as the positive electrode and AC-coated Ni foam as the negative electrode using aqueous 3 M KOH electrolyte and cellulose paper as a dielectric separator material. The mass balancing was attained using eq 3 to get the maximum voltage window and performance and the total mass loading was 1.1 mg cm^{-2}.

$$\frac{m+}{m-} = \frac{C - \Delta V-}{C + \Delta V+} \tag{3}$$

Both CV and GCD were operated in an enhanced potential window range between 0 and 1.7 V. The energy density (E = W h kg^{-1}) and power density (P = W kg^{-1}) were calculated with following eqs 4 and 5, respectively
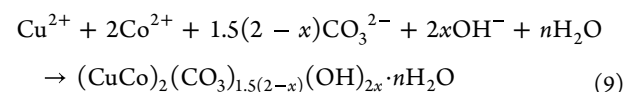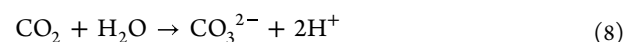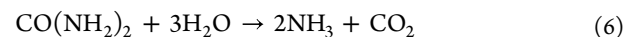
$$E = \frac{I\int_{t1}^{t2} Vt \cdot dt}{M 3.6} \tag{4}$$

$$P = \frac{3600E}{\Delta t} \tag{5}$$

Here, I represents the current applied and potential range after the IR drop in the discharge curve, M represents total mass, and Δt represents the total discharge time.

■ RESULTS AND DISCUSSION

During the course of synthesis, carbonate and hydroxyl anions generated from urea react with copper and cobalt cations (from metal precursor sources) leading to the formation of CCH materials (eqs 6−9).[42,43]

$$CO(NH_2)_2 + 3H_2O \rightarrow 2NH_3 + CO_2 \tag{6}$$

$$NH_3 + H_2O \rightarrow NH_4^+ + OH^- \tag{7}$$

$$CO_2 + H_2O \rightarrow CO_3^{2-} + 2H^+ \tag{8}$$

$$Cu^{2+} + 2Co^{2+} + 1.5(2 - x)CO_3^{2-} + 2xOH^- + nH_2O$$
$$\rightarrow (CuCo)_2(CO_3)_{1.5(2-x)}(OH)_{2x} \cdot nH_2O \tag{9}$$

The double hydroxide grown electrodes are subjected to heat treatment under an air atmosphere resulting in the formation of oxide compounds (CCO), as mentioned below in eq 10.[44]

$$(CuCo)_2(CO_3)_{1.5(2-x)}(OH)_{2x} \cdot nH_2O + O_2$$
$$\rightarrow 2CuCo_2O_4 + 3(2 - x)CO_2 + (2x + 2n)H_2O \tag{10}$$
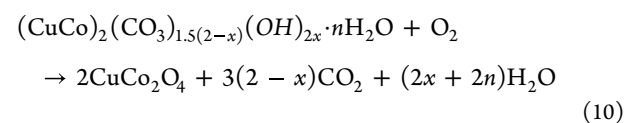
The step-up-wise conversion of oxide to sulfide was achieved hydrothermally with Na$_2$S as a sulfurizing agent, delivering CCS
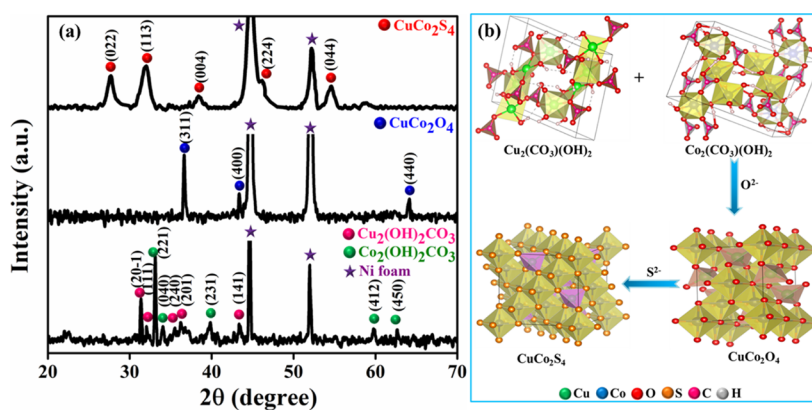
Figure 1. (a) XRD pattern of prepared CCH, CCO, and CCS urchin samples and (b) respective crystal structures.
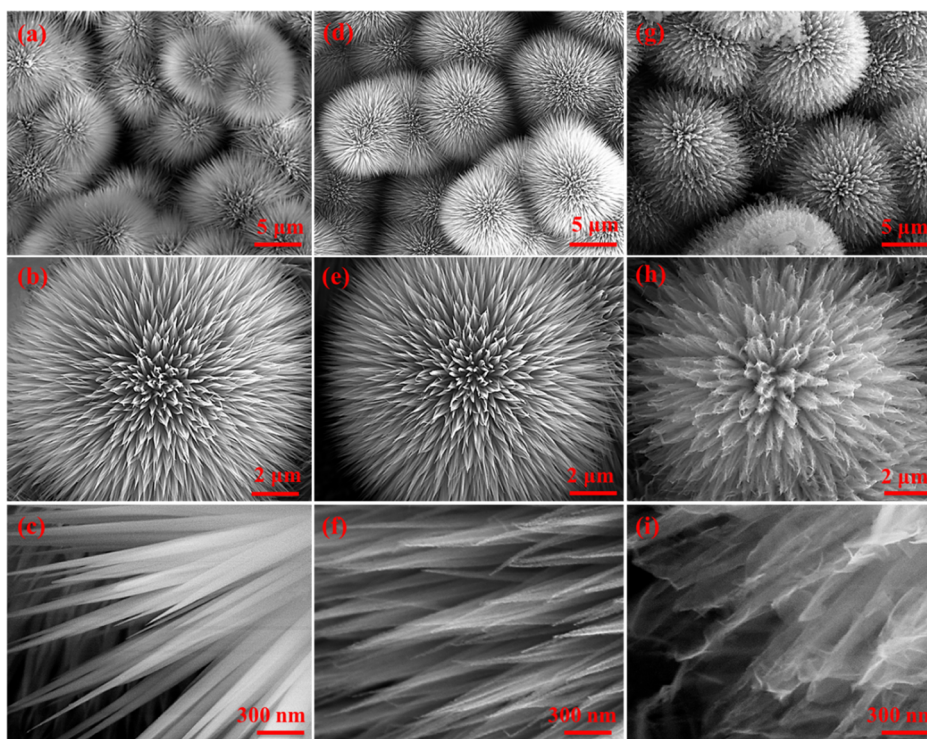

Figure 2. HRSEM images of (a−c) CCH, (d−f) CCO, and (e−i) CCS urchin samples.

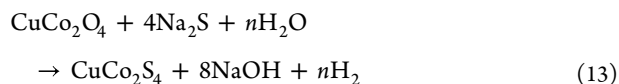materials. The sulfurization reaction mechanism is denoted below in 11,[45,46]

$$Na_2S \rightarrow 2Na^+ + S^{2-} \tag{11}$$

$$S^{2-} + H_2O \rightarrow HS^- + OH^- \tag{12}$$

$$CuCo_2O_4 + 4Na_2S + nH_2O$$
$$\rightarrow CuCo_2S_4 + 8NaOH + nH_2 \tag{13}$$

Figure 1a represents the XRD pattern of fabricated electrodes with common Ni foam substrate peaks at around 44 and 52°. CCH provided a set of peaks representing the presence of $Cu_2(OH)_2(CO_3)$ and $Co_2(OH)_2(CO_3)$. The peaks at 31.3, 31.8, 35.47, 36.25, and 43.35° attributing $(2\bar{0}1)$, (111), (240), (201), and (141) planes, respectively of $Cu_2(OH)_2(CO_3)$ with monoclinic crystalline structure (JCPDS—720075). Orthorhombic structured $Co_2(OH)_2(CO_3)$ contributing (221), (040), (231), (412), and (450) planes, respectively, are represented by peaks at 33.12, 34.05, 39.83, 59.81, and 62.69° (JCPDS—480083). The obtained diffraction peaks at 36.65, 43.36, and 64.15° match with the (311), (400), and (440) crystalline planes, respectively, of spinel $CuCo_2O_4$ material (JCPDS—782177). Formation of $CuCo_2S_4$ has been confirmed with an indication of peaks at 27.67, 32.02, 38.49, 46.21, and 54.49° corresponding to (022), (113), (004), (224), and (044) planes of the spinel crystal structure (JCPDS—421450). The structural and phase transformation due to anion exchange illustrated in Figure 1b explains the change in crystalline nature upon each step. The double hydroxide-based CCH results in single crystalline cubic spinel (AB_2X_4)-structured CCO and CCS with tetrahedral (A = Cu) and octahedral sites (B = Co) possessing multi-valent metal species coordinated with anion atoms (X = O or S).[47−50]

The morphological studies of the prepared electrode materials (CCH, CCO, and CCS) were primarily examined by HRSEM and presented in Figure 2. The homogenous decoration of 3-D spherical urchin microstructures was observed during HRSEM

analysis for prepared materials CCH (Figure 2a), CCO (Figure 2d), and CCS (Figure 2g), with an average size of 3−5 μm. Figure 2b,e,h portrays the individual urchin architecture, consisting of 1-D nanospikes aligned vertically toward the outside in a 3-D manner. The CCH individual spikes morphological details were studied under high resolution, showing the 20−25 nm width spikes with smooth and clean surfaces with sharp tips at the end.

During the conversion process of CCH to CCO, the dehydration process because of thermal treatment creates the pores (Figure 2f). The calculated width of CCO material is ~22 nm. However, Figure 2i reveals a 3-D scaffolded sheet-like nature of nanospikes with an approximate sheet thickness of 6.5 nm, caused by the sulfurization process of CCS materials. The detailed elemental mapping and EDAX of CCS are presented in Figure S1a−e, represents the uniform distribution and quantitative composition of elements (Cu, Co, and S). The urchin consists of a sphere morphology surrounded by the 1-D nanorod array, which forms viz following growth mechanism (Figure 3). The nucleation process of Cu^{2+} and Co^{2+} cations to
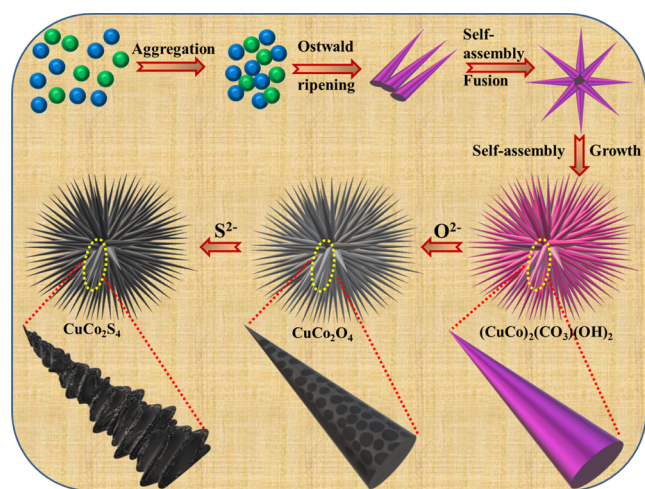

Figure 3. Schematic representation of formation mechanism of CCH urchin and the derivatization steps.

small crystal nuclei was initiated by hydroxy anions produced by the decomposition of urea. The thermodynamically unstable initial nuclei with high surface energy lead to the aggregation process and construct large nuclei by the Oswald ripening process. During the thermal disintegration of urea, the abundant NH_3 was formed, which acts as a capping agent and leads to the formation of nanospikes.[51]

Under a hydrothermal environment at elevated temperatures and pressures, the surface energy of the nanospikes is much higher, deriving the aggregation of individual spikes to bundles to reduce the Gibbs free energy of the whole system.[52] Pertinently, owing to the different electronic environments of Cu^{2+} and Co^{2+} present in hydroxide crystal nuclei, which prefer different growth orientations.[53] Henceforth, the nanospike bundles share a common core, yet radically grow outward, resulting in a sea urchin morphology. The supplemental morphological evolution was brought up by the effect of NH_4F, due to the generation of more active sites by impulsive force between the fluoride anion and Ni foam substrate enhances the uniform growth of urchin structure on the Ni foam substrate.[54] The prepared double hydroxide (CCH) was subjected to thermal decomposition, providing corresponding

oxide materials (CCO) without altering the urchin morphological feature.

During the course of the thermal treatment of CCH, the dehydration process creates pores and enhances the porosity of the material. The anion exchange process was carried out hydrothermally to exchange the $O^{2−}$ to $S^{2−}$ resulting in sulfide, and drove the spikes to become 3-D scaffolded, layered, porous, and with a rough surface in CCS, which can further enhance the morphological features and buffer the volumetric change during ASC performance. Further in-depth analysis of prepared materials (CCO and CCS) were carried out by HRTEM analysis, to understand their morphological advantages and their influence in the electrochemical application. To obtain a perception of urchin microspheres built up of numerous nanospikes, the individual nanospikes were studied. Figure 4a depicts the individual porous CCO nanospikes. The porous nature is clearly pictured in Figure 4b, explaining the arrangement of individual nanoparticles with interparticle voids and spaces, which generates a porous nature to the spikes. The lattice parameters were measured from high-resolution imaging (Figure 4c), the fringes with *d*-spacing values of 0.471, 0.248, and 0.209 nm, attributed to (111), (311), and (400) planes, respectively. Furthermore, Figure 4c provides additional insights on the mesoporous nature of the material by clearly putting on view of interparticle spaces and voids with sizes between 2 and 5 nm. The selected area electron diffraction (SAED) pattern is represented in Figure 4d, explaining the polycrystalline nature of the CCO material. In the case of CCS, Figure 4e displays the low and high-resolution images of nanospikes, elucidates the sheet nature of spikes, which is swiveled in a uni-direction, and forms a 3-D scaffolded architecture with intersheet spaces, voids, and with corrugation on edges. Under the electron beam, the gauze-like, flexible, and transparent nature of the nanosheet was observed, which indicates the ultrathin thickness of sheets on the edges of the nanospike. The dark zones are demonstrating the folded, crinkled, and stacking of ultrathin sheets, which creates ion transportation channels and spaces.[55] The obtained lattice spacings were 0.286, 0.236, and 0.193 nm (Figure 4g), corresponding to (113), (004), and (224) planes of CCS materials, which also communicate about the intersheet areas and flake-like nature of sheets. Figure 4h illustrates the SAED pattern of the CCS material, exhibiting the polycrystalline nature as well.

The surface area analysis of prepared materials (CCH, CCO, and CCS) was performed by the BET technique, resulting in a type-IV isotherm hysteresis loop (Figure 4i), which is attributing the mesoporous nature of the materials as predicted through HRTEM previously. The increment in the surface area while converting hydroxide to oxide to sulfide was quantitatively attained (Figure 4k), as CCH, CCO, and CCS provides 23.9, 30.1, and 40.5 m^2 $g^{−1}$, evidently explicating the effect of morphological transformation.

BJH analysis provides details related to the porosity of the materials (Figure 4j). The mesoporosity was obviously established through the obtained pore radius of 3.7, 5.5, and 5.9 nm, respectively, to CCH, CCO, and CCS materials (Figure 4k). The obtained BET results state the fact that primarily CCH possesses less surface area and porosity, development is brought up by converting it to oxide viz thermal treatment. As discussed earlier, the respective dehydration and decarboxylation processes during oxide formation creates enormous porosity in the material, which is evinced by the BJH experiment and in
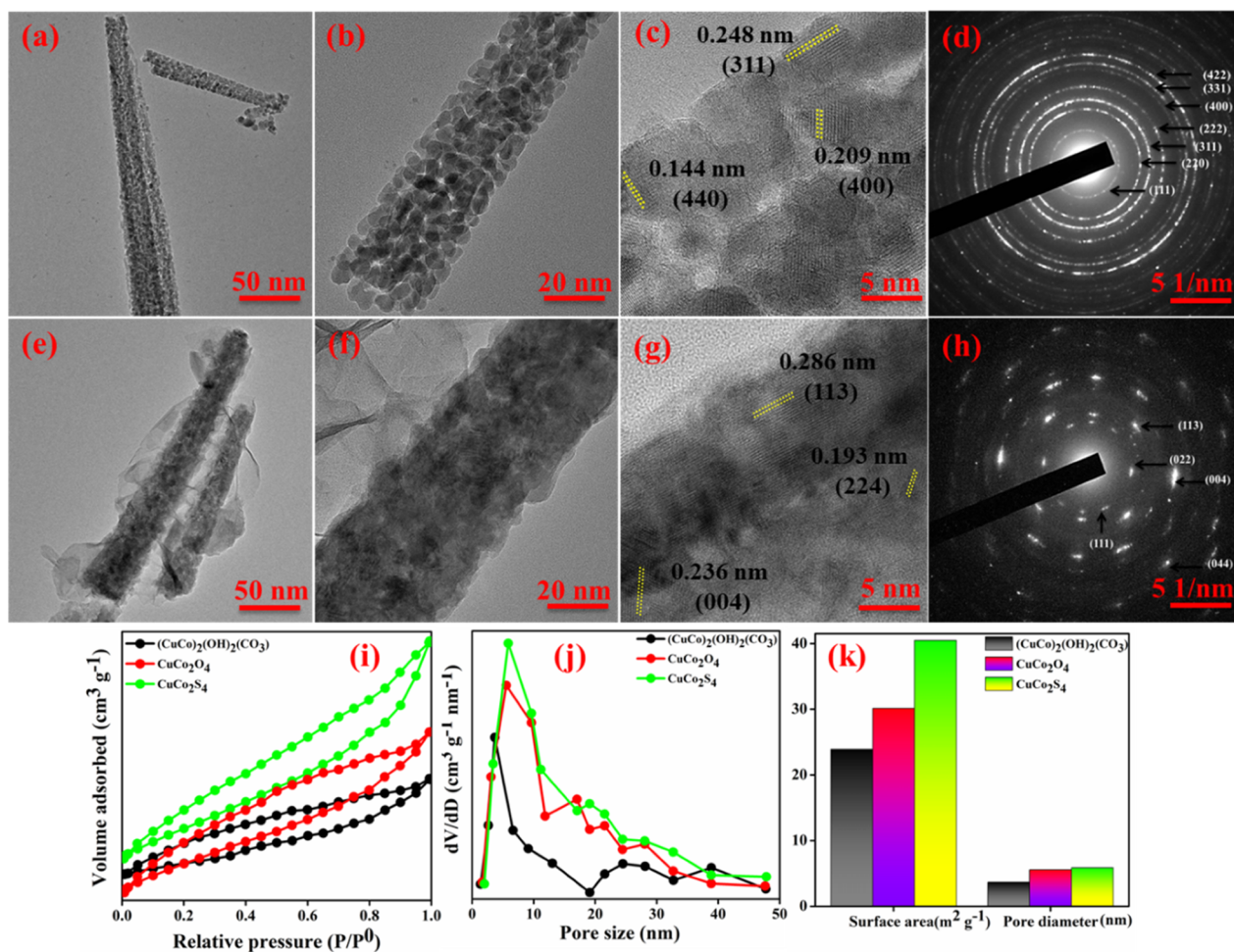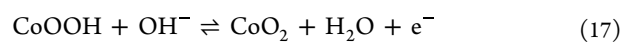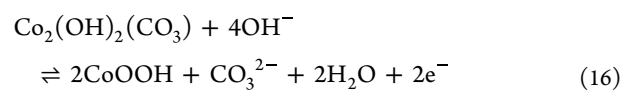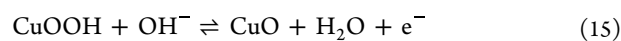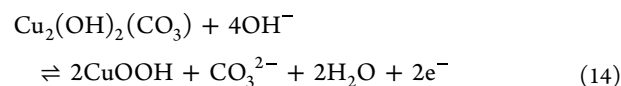
Figure 4. HRTEM images of (a−d) CCO, (e−h) CCS urchin needle array, and (i) nitrogen adsorption−desorption isotherms, (j) BJH pore size distribution analysis, and (k) comparative histogram of BET analysis of CCH, CCO, and CCS urchin samples.

the form of increasing surface area in BET. Upon converting to sulfide, further improvement in the surface area and porosity was achieved with a hierarchical 3-D sheet architecture, clearly supporting the morphological analysis (HRSEM and HRTEM) results and satisfying the conceptuality of proposed mechanisms and interpretations. Hence, it is clear that the designed systematic experimental protocol provided an adequate improvement in the surface area of the material without harming the architecture, which can provide immense electrochemical advantages during the charge storage phenomena.

XPS analysis was further conducted to probe the valence states and surface chemical compositions of the material CCS. The survey spectrum (Figure 5a) exhibited peaks at 952.82, 779.89, and 168.19 eV, corresponding to Cu, Co, and S elements of CCS materials. Emission spectra of Cu 2p were fitted into two peaks corresponding to Cu $2p_{3/2}$ and Cu $2p_{1/2}$ at 932.67 and 952.49 eV with 19.82 splitting energy, which refers to the paramagnetic Cu state (Figure 5b). Deconvoluted spectra of Co 2p consist of twin spin−orbit doublets at 781.18 and 796.59 eV of Co $2p_{3/2}$ and Co $2p_{1/2}$ orbitals of cobalt ion and the splitting energy value of 15.41 eV denotes the existence of both Co^{2+} and Co^{3+} (Figure 5c) in CCS thiospinel compounds. S 2p provided a doublet peak at 162.27 eV, respective to S $2p_{1/2}$ (163.08 eV) and S $2p_{3/2}$ (161.95 eV), and a free sulfate peak at 168.89 eV present in the thiospinel crystalline structure.[56]

Based upon the brief morphological and structural studies of the fabricated electrode, a novel CCS electrode was developed from CCH with improved architecture and features. Whereas, the influence of systematic structural, chemical, and morphological changes as an effect of different ligand systems (OH^-, O^{2-}, and S^{2-}) on their electrochemical properties was studied individually by CV, GCD, and EIS. Distinctive Faradaic characteristics were observed in a three-electrode configuration between a potential range of 0.0 to 0.7 V vs Ag/AgCl at increasing scan rates from 5 to 100 mV s^{-1}. As presented in Figure 6a., CCH exhibited a pair of anodic peaks at 0.49 and 0.56 V vs Ag/AgCl and a cathodic peak at 0.41 V vs Ag/AgCl, attributed to the Cu^{2+}/Cu^{3+} and Co^{2+}/Co^{3+} redox species in double hydroxide material CCH (eqs 14−17).[57,58]

$$Cu_2(OH)_2(CO_3) + 4OH^-$$
$$\rightleftharpoons 2CuOOH + CO_3^{2-} + 2H_2O + 2e^- \tag{14}$$

$$CuOOH + OH^- \rightleftharpoons CuO + H_2O + e^- \tag{15}$$

$$Co_2(OH)_2(CO_3) + 4OH^-$$
$$\rightleftharpoons 2CoOOH + CO_3^{2-} + 2H_2O + 2e^- \tag{16}$$

$$CoOOH + OH^- \rightleftharpoons CoO_2 + H_2O + e^- \tag{17}$$
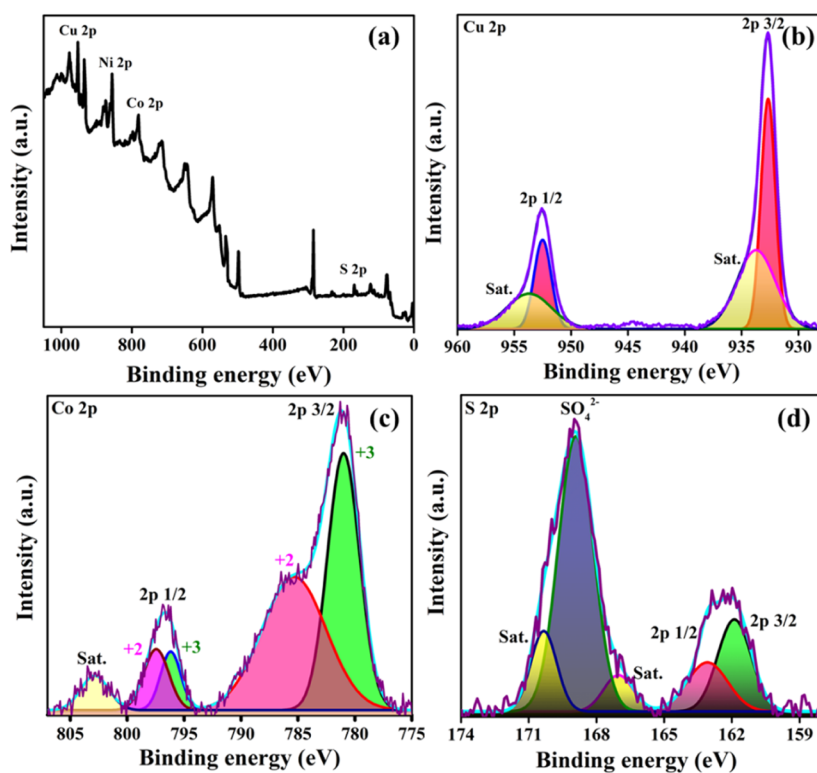
Figure 5. (a) Wide range XPS results of CCS urchin and (b−d) deconvoluted spectrum of Cu 2p, Co 2p, and S 2p elements.
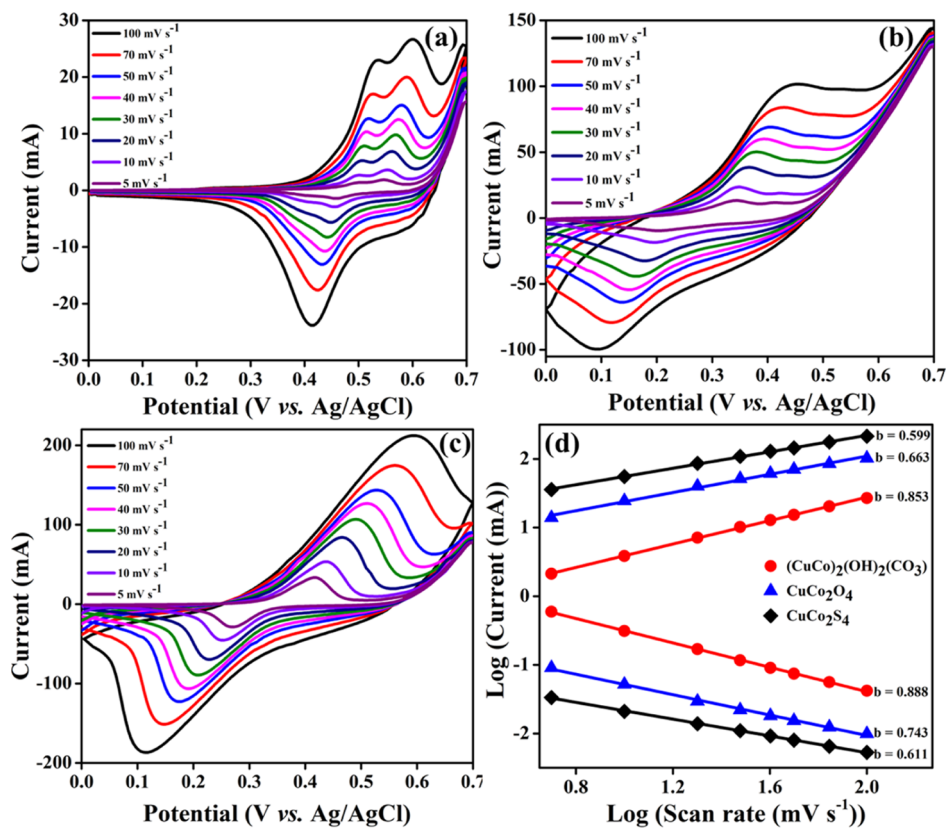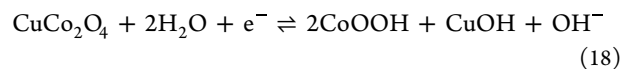

Figure 6. CV of (a) CCH, (b) CCO, and (c) CCS urchin electrodes in 3 M KOH at different scan rates (5−100 mV s^{-1}) and (d) plot of log of peak currents as a function of log of scan rate.

Figure 6b represents the CV curves of oxide materials (CCO), with Cu$^+$/Cu^{2+} and Co^{3+}/Co^{4+} states providing faradic redox peaks at 0.43 and 0.1 V vs Ag/AgCl (eqs 18−20)[59]

$$CuCo_2O_4 + 2H_2O + e^- \rightleftharpoons 2CoOOH + CuOH + OH^-$$
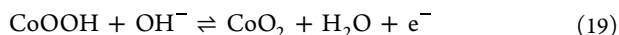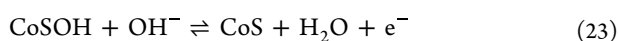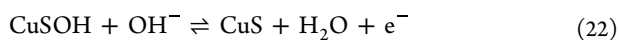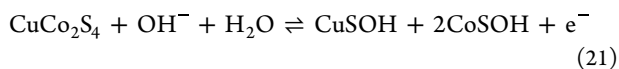
$$(18)$$
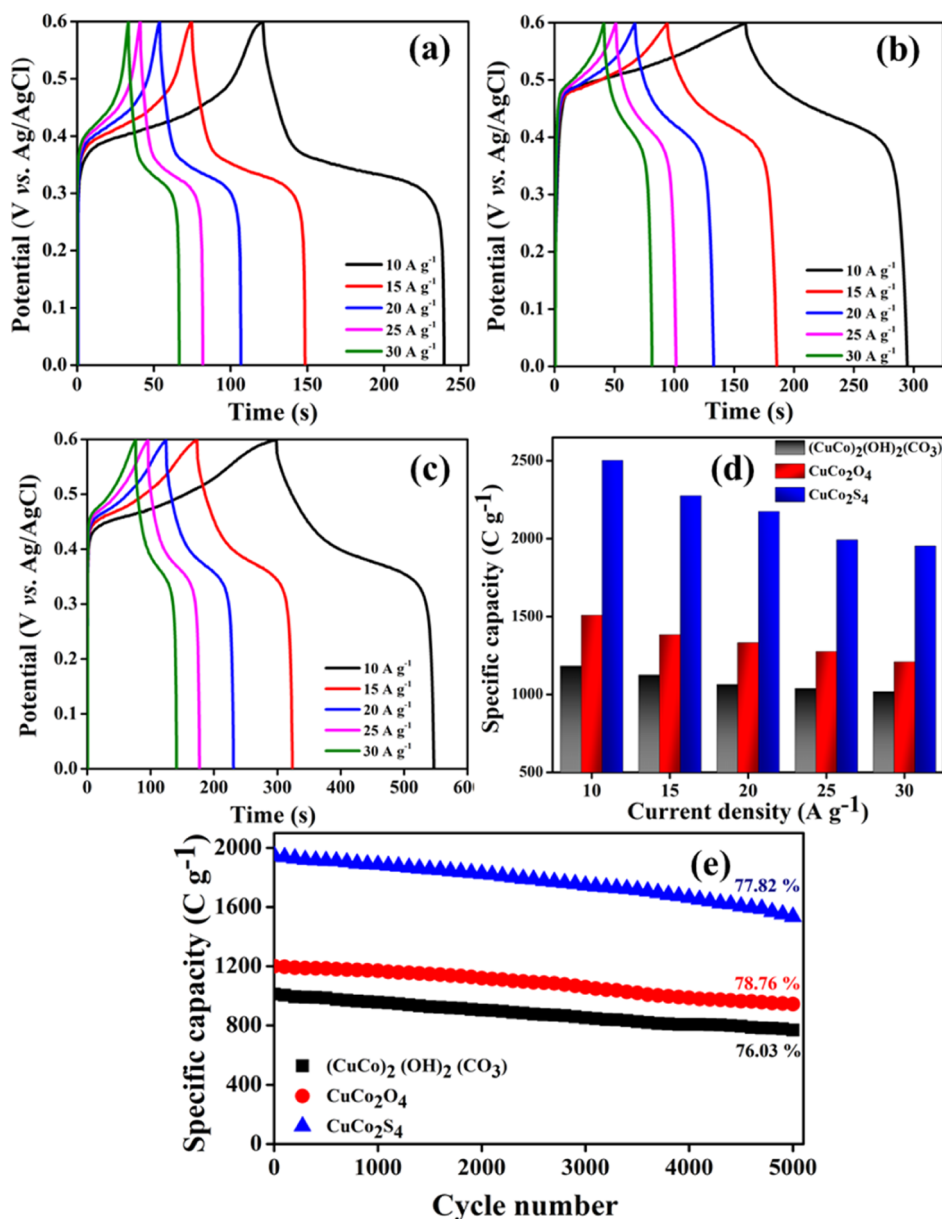
Figure 7. GCD curves of (a) CCH, (b) CCO, and (c) CCS electrodes in 3 M KOH at 10−30 A g^{-1} current density and (d) capacity profiles at respective current densities and (e) cycling performance of electrodes in 3 M KOH at 30 A g^{-1}.

$$CoOOH + OH^- \rightleftharpoons CoO_2 + H_2O + e^- \quad (19)$$

$$CuOH + OH^- \rightleftharpoons Cu(OH)_2 + e^- \quad (20)$$
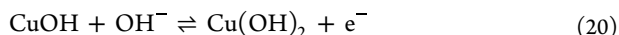
The conspicuous pseudocapacitive behavior was observed for the sulfide material (CCS) with redox peaks at 0.59 and 0.11 V vs Ag/AgCl (Figure 6c), designated to the faradaic reaction of Co^{4+}/Co^{3+} and Cu^{2+}/Cu^+ species, as mentioned in eqs 21−23.[60]

$$CuCo_2S_4 + OH^- + H_2O \rightleftharpoons CuSOH + 2CoSOH + e^- \quad (21)$$

$$CuSOH + OH^- \rightleftharpoons CuS + H_2O + e^- \quad (22)$$

$$CoSOH + OH^- \rightleftharpoons CoS + H_2O + e^- \quad (23)$$

The increasing peak current and area in the obtained CV results efficiently indicate the importance and influence of morphological and structural transformation as an effect of anion exchange. While CCH provides adequate electrochemical activity, the derivatization process triggers the porosity and enlarges active sites in CCO, which improves the electrochemical performance to a better level. The pores generated through decarboxylation and dehydration reactions act as a reservoir for ion/electron transportation and accommodation in CCO. In addition, the interconnected nanoparticle array in nanospikes of CCO urchin architectures creates a better electron hopping environment, which was mirrored by increasing the conductivity (peak current) value.[61] However, further phase transformation with sulfide anions possesses a much-extended impact on electrochemical and conductivity behavior, due to the lower electronegativity and greater covalency of sulfide anions along with the synergistic effect of multi-metal redox species. In particular, the 3-dimensionally twisted 1-D nanospikes of CCS with 2-D porous nanosheets constitute of tremendous sharp tips, scaffolds, angle edges, steps, and corners, offering fluent channels for electrolyte diffusion and adsorption.[62]
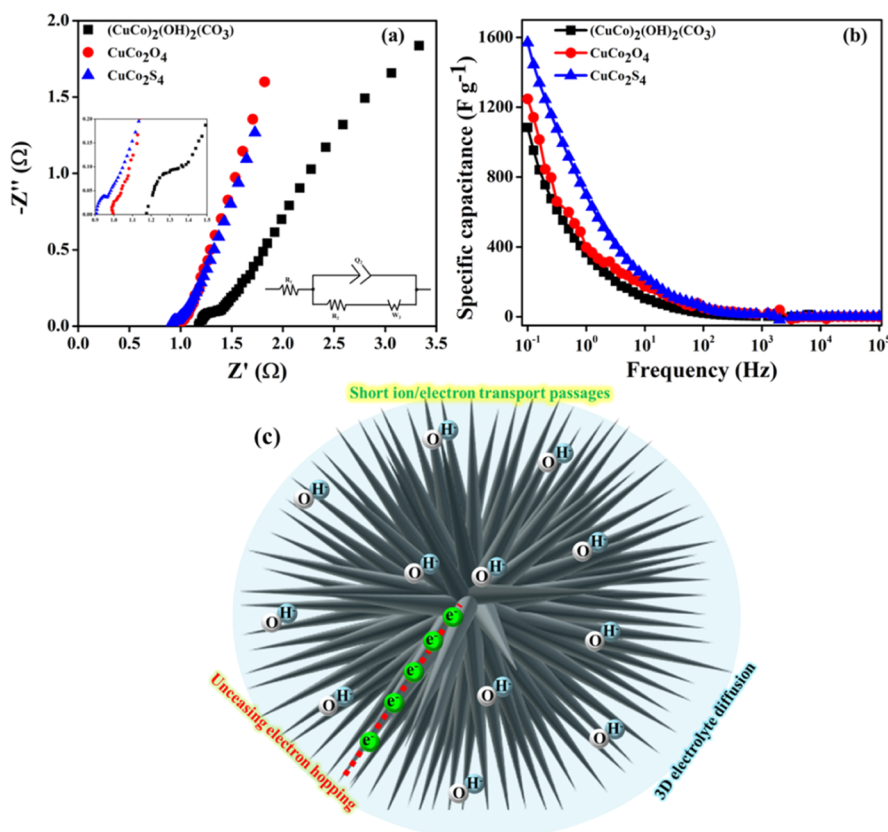
Figure 8. (a) Nyquist plots of CCH, CCO and CCS electrodes before cycling testing, (b) frequency-dependent specific capacitance profile of the electrodes, and (c) pictorial representation of 3D urchin nanostructure electrochemical influence.

The significant redox characteristics even at higher scan rates were defined by the stable increment in the peak area and current with increasing sweep rate. It is noteworthy to denote that among the various reports using F g^{-1} as the unit to quantify the capacity behavior, recent reports are using C g^{-1} and mA h g^{-1} units to describe the performances.[63] The major difference can be brought out by the clarification of electrode material behavior, either capacitive or faradaic, which was determined using the following eq 24

$$\log Ip = b \log \nu + \log a \qquad (24)$$

here, Ip, ν, and a and b are designated to peak current, scan rate, and variable parameters, respectively.[64] The "b" values are derived from eq 19 and portrayed in Figure 6d, indicating the diffusion-controlled processes and affirms the Faradaic character of prepared electrode materials. The charge storage phenomena of electrode materials were evaluated with the GCD method at an applied current density range of 10−30 A g^{-1} (Figure 7a−c). Among the prepared electrodes, CCS provided a maximum specific capacity of 2502 C g^{-1} at 10 A g^{-1} current density, where CCO and CCH deliver 1508 and 1182 C g^{-1}, respectively, indicating the superior capacitive behavior of sulfide material (Figure 7d). Furthermore, even at high applied current density (30 A g^{-1}), the fabricated electrodes CCH, CCO, and CCS exhibited capacity values of 1018.2, 1209.3, and 1953 C g^{-1}, respectively. The stability test was conducted to evaluate the durability of prepared electrodes under the electrochemical condition at a high current density of 30 A g^{-1}. The obtained results indicate that CCH, CCO, and CCS provided retention values of 76.03, 78.76, and 77.82% compared to their initial

capacity value, pronouncing the improvised rate capability of binder-free redox-based electrode materials in PC applications.

The comprehensive kinetics and charge-transfer mechanism studies were conducted viz EIS measurements for each electrode between the frequency range of 100 kHz to 100 mHz at an applied bias of 0 V. Figure 8a shows a Nyquist plot of prepared electrodes, fitted with Randles equivalent circuit, and the electrical parameters are tabulated in Table S1. Owing to the contact resistance at the electrode/electrolyte interface, the solution resistance (R_s) arises at higher frequency regions in values of 1.181, 0.996, and 0.906 Ω for CCH, CCO, and CCS materials, respectively. The charge-transfer resistance (R_{ct}) was derived from the diameter of the semicircle at a higher frequency region, delivering details on redox reaction kinetics at the electrode interface.

Among the prepared electrodes, the CCS electrode governed a minimal R_{ct} value of 0.087 Ω, where CCO and CCH presented 0.103 and 0.281 Ω, explaining the rapid ion transportation and superior charge storage capability of CCS material. The frequency-dependent capacity behavior of electrode materials is represented in Figure 8b, and the maximum capacitive values were obtained at a lower frequency as the higher frequency region restricts the surface process due to the shorter permeation length of AC voltage.[65] At 0.1 Hz frequency, the maximum specific capacitance values observed are 1598, 1251, and 1008 F g^{-1} for CCS, CCO, and CCH materials. The capacitance values obtained from EIS particularly explain differential capacity differs from GCD, which measures differential and integral capacity together. In PCs, the GCD-derived capacities are valued corresponding to the device assembly and performance analysis, where EIS-derived
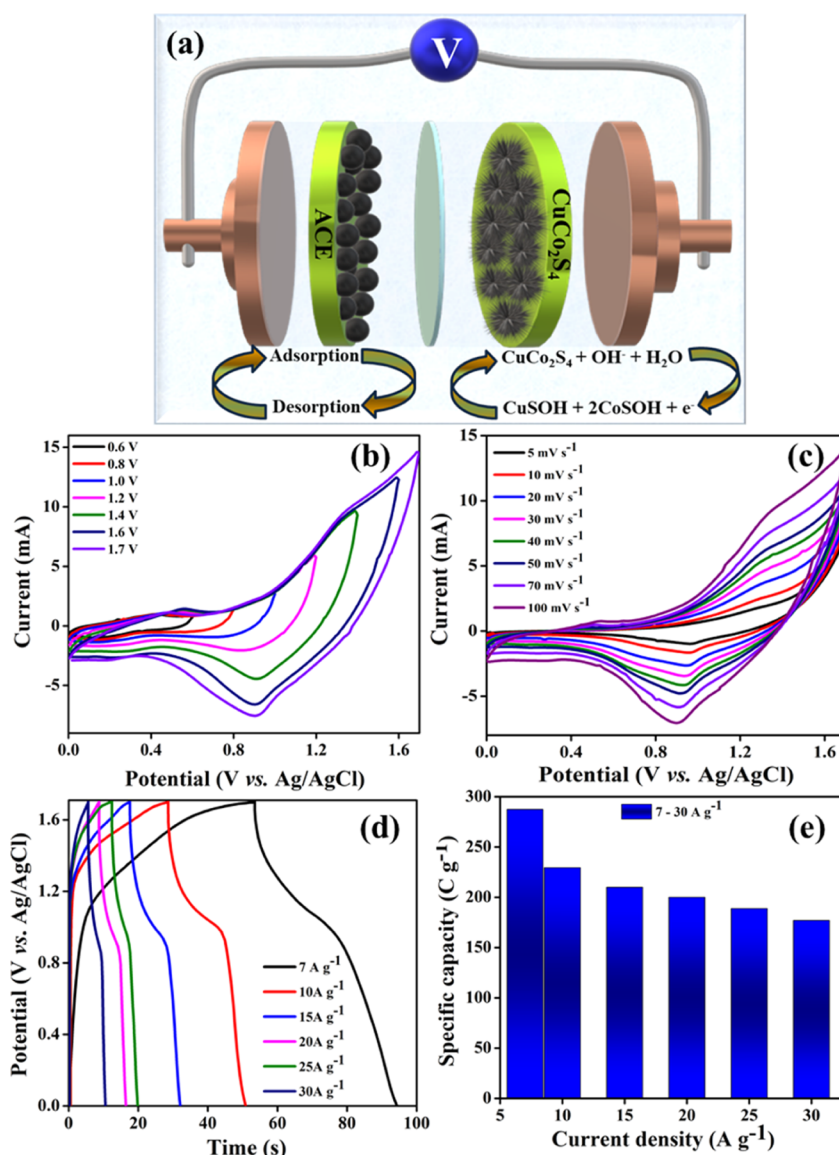
Figure 9. Device performance results of the CCS//AC cell (a) device assembly, (b) CV curves as a function of increasing potential window from 0.6 to 1.7 V at 100 mV s^{-1}, (c) CV curves at different scan rates ranging 5−100 mV s^{-1}, (d) GCD curves at 10−30 A g^{-1} applied current density, and (e) respective capacity profiles.

capacitance provides exclusive knowledge on the relationship between electrode kinetics and their corresponding capacitive behavior.[66] After the stability test, EIS was recorded (Figure S2), the slight increment in the resistance values because of electrochemical processes is tabulated in Table S1. The interpenetrating architecture of 3D urchin microstructures with infinite 2D nanospikes has shown a potential effect on electrochemical activity (Figure 8c). The authentic 3D morphology offers enhanced surface area and conductivity by offering multi-dimensional electrolyte diffusion passage, ample space for electron/ion transportation and accommodation, and increases the redox activity and specific capacity behavior into a greater level.

To encounter the real-world application, the hybrid cell was assembled using superior functioning CCS as the cathode and ACE as the anode under aqueous electrolytic conditions (3 M KOH) (Figure 9a). The mass ratio, voltage range, and current density ranges were systematically optimized toward achieving a better performing PC device with higher energy and power

density values. The CV studies were conducted at increasing the potential range from 0.6 to 1.7 V at 100 mV s^{-1} scan rate, to attain the optimum operating potential window range for the constructed asymmetric cell (Figure 9b). The resultant CV clearly pictures the hybrid nature of cell with EDLC and redox behavior at lower and higher potential ranges, respectively. As a function of increasing scan rate from 5 to 100 mV s^{-1} (Figure 9c), the CV resulted significant redox behavior, indicating the high reversibility and lower polarization of assembled cell at a potential range of 1.7 V. Capacity phenomena were analyzed with GCD measurements at applied current density ranging from 7 to 30 A g^{-1} (Figure 9d), resulting in a higher specific capacity value of 287.35 C g^{-1} at 7 A g^{-1} and provides 177 C g^{-1} even at a high current density of 30 A g^{-1} with 61.6% retention value (Figure 9e).

To analyze the long-term durability of the cell, the stability test was conducted at 30 A g^{-1} current density for 5000 cycles (Figure 10a), exhibiting the superior charge/discharge performance with 94.2% capacity retention. The initial and final GCD
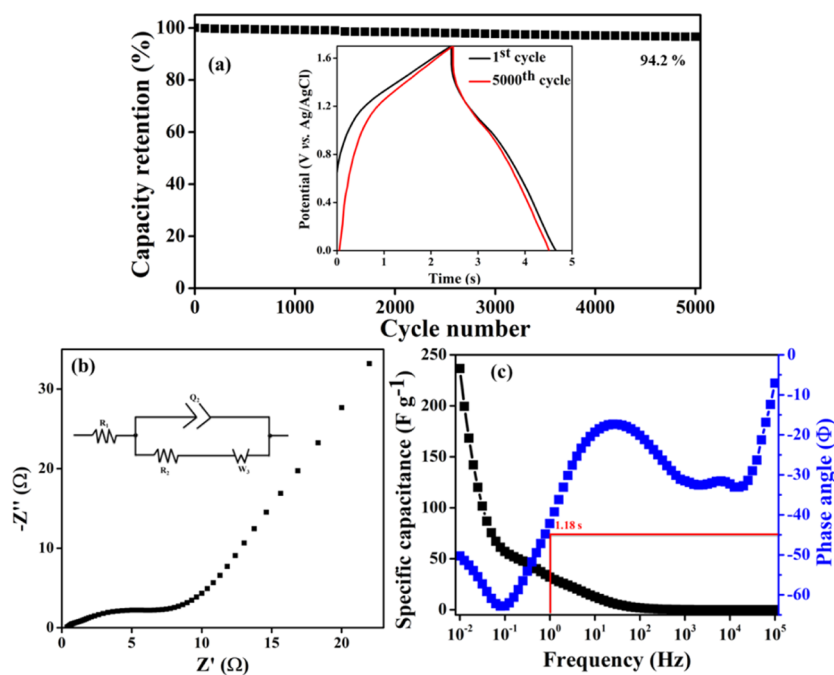
Figure 10. (a) Cycling test at 30 A g^{-1} (inset shows the initial and final GCD curves), (b) Nyquist plot of CCS//AC before cycling (inset: respective equivalent circuit), and (c) capacitance and phase angle profile at a fixed range of frequency.
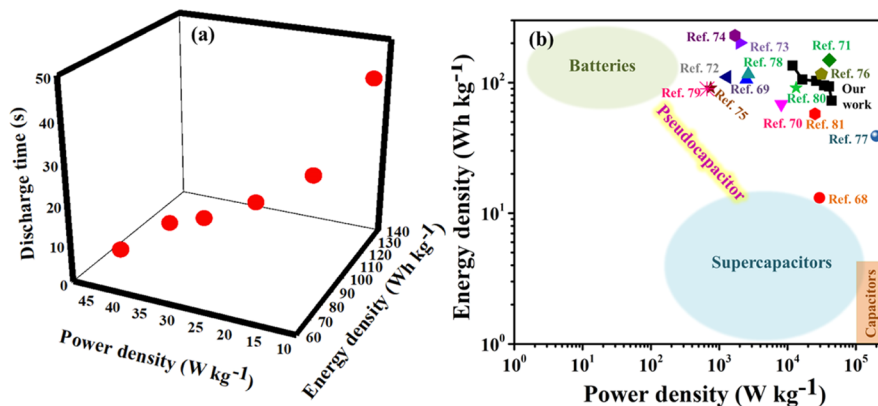

Figure 11. Ragone plot of fabricated CCS//ACE asymmetric cell (a) at different applied current densities (7−30 A g^{-1}) and (b) comparative studies with reported faradaic PCs.

profiles are presented in Figure 10a; the inset shows the unaltered and stable capacity behavior of the cell from the 1st to 5000th cycle, which exhibits the astonishing rate capability and cycling performance of the CCS//ACE device.

EIS analyses were done to get details on charge-transfer and resistance properties of fabricated devices, CCS//ACE. Figure 10b represents the Nyquist plot of device with R_s and R_{ct} values of 0.316 and 10.947 Ω, highlights the proper interfacial conductance between CCS and ACE with high electron conductivity, mass-transfer, and rate performance properties of cells. The Bode plot was taken into account to elucidate the correlation between the phase angle and capacitance of the constructed CCS//ACE PC device at a fixed frequency range (10 mHz to 100 kHz) (Figure 10c). The minimal discharge time requirement can be estimated with the relaxation time (τ_0), which is obtained from the frequency range where the phase angle hits −45° called knee frequency (f_0).[67] As f_0 and τ_0 are inversely proportional to each other, the obtained τ_0 1.18 s articulates the efficient charge storage capability of the device

with a maximum capacitance value of 247.81 F g^{-1}. Impedance studies are carried out after the long-term cycling and portrayed in Figure S3, explaining a fact that despite the slight increment in the R_s value (0.632 Ω) due to the electrochemical environment, there is a huge decrement in the R_{ct} value as 4.234 Ω. The drastic decrement in charge-transfer resistance indicates the activation process that happened during the charge/discharge phenomena due to the insertion of OH$^-$ ions, which improvise the wettability, adsorption, and mass-transfer processes subsequently decrease the R_{ct} value of the device.

The energy and power density are assessed with the Ragone plot at a different current density of 7 to 30 A g^{-1} (Figure 11a). The obtained graph shows that the fabricated CCS//ACE cell provided a high energy density value of 135.3 W h kg^{-1} at 11.87 kW kg^{-1} on 7 A g^{-1} current density. Upon increasing the current density constructed system sustained to produce stable energy, at a higher applied current density (30 A g^{-1}) value of 72.68 W h kg^{-1}, specific energy was harvested, even with an ultra-high power density of 44.35 kW kg^{-1}. To estimate the practical

Table 1. Comparison Table of Electrochemical Performances of ASC Devices Based on Faradaic Electrode Materials[a]

cathode material	power density (kW kg^{-1})	energy density (W h kg^{-1})	cycling performance and retention %	refs
GCNAS	13.1	29.4	10,000 and 92.8	68
RGO/CuS	105.6	2.5	5000 and 89	69
CuS/TiO$_2$	68.4	8.1	25,000 and 87	70
porous graphene	148.75	41	7000 and 100	71
C@Mn$_3$O$_4$	110.4	1.3	10,000 and 100	72
MnMoO$_4$/graphene	202.2	2	1000 and 88	73
NACs	230	1.7	8000 and 76.3	74
NiCo$_2$Al-LDH	91	0.75	5000 and 92	75
Zn-aMEGO	106.3	31.4	80,000 and 93	76
3-D carbon	39	200	10,000 and 92	77
VS$_4$/rGO/CoS$_2$@Co	106	2.67	2000 and 93.3	78
CuCo$_2$S$_4$	0.663	89.6	10,000 and 91.5	79
CuCo$_2$O$_4$	13.4	91.4	5000 and 92.32	80
La$_{0.85}$Sr$_{0.15}$MnO$_3$@NiCo$_2$O$_4$	57.6	25.2	10,000 and 100	81
Zn$_{0.25}$Ni$_{0.75}$Co-LDH	0.789	51.8	10,000 and 94.6	82
Co−NiWO$_4$	1.7	42.2	15,000 and 93.5	83
NiFeCo LDH	0.935	34.4	15,000 and 99	84
Zn$_{0.5}$Co$_{0.5}$S	0.957	49	10,000 and 88	85
CuCo$_2$S$_4$	**11.87**	**135.3**	**5000 and 94.2**	**this work**

[a]Here, GCNAS = sulfurized CoNiAl LDHs (CoNiAlLDH) embedded in graphene nanosheets, GCFS = graphene nanosheet/Co$_{0.33}$Fe$_{0.67}$S$_2$ composite, NACs = nitrogen-doped activated carbons, LDH = layered double hydroxide, and aMEGO = porous carbon derived from chemical activated graphene.

applicability of developed cathode materials, the obtained energy and power density values are correlated with previous reports and represented in Figure 11b.[68−85] Among the various reports Li et al. have reported a carbon electrode-based SC device with a high energy density value of 230 W h kg^{-1} at 1.7 kW kg^{-1} power density value.[74] The transition-metal-based electrode (MnMoO$_4$/graphene) was developed to give 202.2 W h kg^{-1} energy density at 2 kW kg^{-1}, as studied by Ghosh et al.[73] and Zhao et al. who developed CoS$_2$ rGO-based electrode and a harvested energy density of 105.6 W h kg^{-1} and 2.5 kW kg^{-1} power density value.[69] The highest power density value was produced by an activated mesoporous carbon-based electrode designed and developed by Li et al., as in a value of 200 kW kg^{-1} with a corresponding energy density of 39 W h kg^{-1}.[77] Thus, the fabricated CCS//ACE cell with the developed CuCo$_2$S$_4$ urchin cathode yielded energy density far better than conventional SCs also near the value of commercial batteries and superior power density than batteries, satisfying the concept of constructing asymmetric PC devices. For better knowledge, the results are compared with previously reported devices, as listed in Table 1.

CONCLUSIONS

The CDH-based electrode material was prepared by a simple hydrothermal procedure. The synthetic advantages provided a well-designed,3-D spatial urchin architecture, followed by the anion exchange processes toward deriving the most functioning oxide and sulfide-based electrode materials. Among the prepared materials, CuCo$_2$S$_4$ (CCS) provided the highest specific capacity value (2502 C g^{-1} at 10 A g^{-1}) and electrochemical performances were appealing even at higher current density values. The advantages of electrode material were not only governed by multi-redox metal species and labile sulfur atoms but also by the morphological merits of the electrode with rough, porous, scaffolded, hierarchical architectures. Based on three electrode results, the asymmetric PC device was assembled with CCS as a cathode, providing a specific capacity value of 287.35 C g^{-1} at 7 A g^{-1} and 94.2%

capacity retention after 5000 cycles at a high current density of 30 A g^{-1}. The efficiency of the developed electrode was analyzed by the energy and power density values of the cells, which demonstrated high energy and power density values of 135.3 W h kg^{-1} (at 7 A g^{-1}) and 44.35 kW kg^{-1} (30 A g^{-1}). Henceforth, the systematic derivatization of CDH-based electrode material has resulted in a superior impact on the development of electrode materials based on a facile and effective anion exchange process with high energy and power density values for commercial applications of PCs.

ASSOCIATED CONTENT

ⓢ Supporting Information

The Supporting Information is available free of charge at https://pubs.acs.org/doi/10.1021/acsomega.3c01211.

HRSEM elemental mapping and EDAX spectrum of CCS; Nyquist plots of CCH, CCO, and CCS after cycling studies; electrical parameters for CCH, CCO and CCS before and after cycling studies from EIS measurements; Nyquist plots of CCS//AC device after electrochemical testing; and electrical parameters of CCS//AC devices before and after electrochemical testing (PDF)

AUTHOR INFORMATION

Corresponding Author

Manab Kundu − *Electrochemical Energy Storage Laboratory, Department of Chemistry, SRM Institute of Science and Technology, Chennai, Tamil Nadu 603203, India;* ⓞ orcid.org/0000-0002-5707-3118; Email: manabm@srmist.edu.in, chemmanab@gmail.com

Author

Amala George − *Electrochemical Energy Storage Laboratory, Department of Chemistry, SRM Institute of Science and Technology, Chennai, Tamil Nadu 603203, India*

Complete contact information is available at:

■ REFERENCES

(1) Chao, D.; Zhou, W.; Xie, F.; Ye, C.; Li, H.; Jaroniec, M.; Qiao, S. Z. Roadmap for advanced aqueous batteries: From design of materials to application. *Sci. Adv.* **2020**, *6*, No. eaba4098.

(2) Simon, P.; Gogotsi, Y. Materials for electrochemical capacitors. *Nat. Mater.* **2008**, *7*, 845−854.

(3) Zhang, G. C.; Feng, M.; Li, Q.; Wang, Z.; Fang, Z.; Niu, Z.; Qu, N.; Fan, X.; Li, S.; Gu, J.; Wang, J.; Wang, D. High energy density in combination with high cycling stability in hybrid supercapacitors. *ACS Appl. Mater. Interfaces* **2022**, *14*, 2674−2682.

(4) Wang, W.; Xiao, Y.; Li, X.; Cheng, Q.; Wang, G. Bismuth Oxide Self-Standing Anodes with Concomitant Carbon Dots Welded Graphene Layer for Enhanced Performance Supercapacitor-Battery Hybrid Devices. *Chem. Eng. J.* **2019**, *371*, 327−336.

(5) Zhao, W.; Zheng, Y.; Cui, L.; Jia, D.; Wei, D.; Zheng, R.; Barrow, C.; Yang, W.; Liu, J. MOF derived Ni-Co-S nanosheets on electrochemically activated carbon cloth via an etching/ion exchange method for wearable hybrid supercapacitors. *Chem. Eng. J.* **2019**, *371*, 461−469.

(6) Chen, J.; Xu, W.; Wang, H.; Ren, X.; Zhan, F.; He, Q.; Wang, H.; Chen, L. Emerging two-dimensional nanostructured manganese-based materials for electrochemical energy storage: recent advances, mechanisms, challenges, and prospects. *J. Mater. Chem. A* **2022**, *10*, 21197−21250.

(7) Zhan, F.; Wang, H.; He, Q.; Xu, W.; Chen, J.; Ren, X.; Wang, H.; Liu, S.; Han, M.; Yamauchi, Y.; Chen, L. Metal−organic frameworks and their derivatives for metal-ion (Li, Na, K and Zn) hybrid capacitors. *Chem. Sci.* **2022**, *13*, 11981−12015.

(8) Chen, X.; Li, C.; Grätzel, M.; Kostecki, R.; Mao, S. S. Nanomaterials for renewable energy production and storage. *Chem. Soc. Rev.* **2012**, *41*, 7909−7937.

(9) Zhang, X.; Tian, X.; Liu, C.; Qiao, J.; Liu, W.; Liu, J.; Zeng, Z. MnCo-MOF-74 derived porous MnO/Co/C heterogeneous nanocomposites for high-efficiency electromagnetic wave absorption. *Carbon* **2022**, *194*, 257−266.

(10) Liu, C.; Qiao, J.; Zhang, X.; Yang, Y.; Li, B.; Wu, L.; Liu, W.; Zeng, Z.; Liu, J. Noncovalent self-assembly of a minuscule amount of nickel porphyrin on carbon nanotube for high-performance electromagnetic wave absorbing. *Composites, Part A* **2023**, *164*, 107281.

(11) Tian, H.; Qiao, J.; Yang, Y.; Xu, D.; Meng, X.; Liu, W.; Zhang, X.; Li, B.; Wu, L.; Zeng, Z.; Liu, J. ZIF-67-derived Co/C embedded boron carbonitride nanotubes for efficient electromagnetic wave absorption. *Chem. Eng. J.* **2022**, *450*, 138011.

(12) Wang, C. H.; Zhang, X.; Xu, Z. T.; Sun, X. Z.; Ma, Y. W. Ethylene Glycol Intercalated Cobalt/Nickel Layered Double Hydroxide Nanosheet Assemblies with Ultrahigh Specific Capacitance: Structural Design and Green Synthesis for Advanced Electrochemical Storage. *ACS Appl. Mater. Interfaces* **2015**, *7*, 19601−19610.

(13) Xu, W.; Zhao, X.; Zhan, F.; He, Q.; Wang, H.; Chen, J.; Wang, H.; Ren, X.; Chen, L. Toward emerging two-dimensional nickel-based materials for electrochemical energy storage: Progress and perspectives. *Energy Storage Mater.* **2022**, *53*, 79−135.

(14) Wang, H.; Ren, X.; Chen, J.; Xu, W.; He, Q.; Wang, H.; Zhan, F.; Chen, L. Recent advances of emerging oxyhydroxide for electrochemical energy storage applications. *J. Power Sources* **2023**, *554*, 232309.

(15) Xu, P.; Ye, K.; Du, M.; Liu, J.; Cheng, K.; Yin, J.; Wang, G.; Cao, D. One-step synthesis of copper compounds on copper foil and their supercapacitive performance. *RSC Adv.* **2015**, *5*, 36656−36664.

(16) Xiao, J. W.; Wan, L.; Yang, S. H.; Xiao, F.; Wang, S. Design hierarchical electrodes with highly conductive NiCo$_2$S$_4$ nanotube arrays grown on carbon fiber paper for high-performance pseudocapacitors. *Nano Lett.* **2014**, *14*, 831−838.

(17) Deshmukh, A. D.; Urade, A. R.; Nanwani, A. P.; Deshmukh, K. A.; Peshwe, D. R.; Sivaraman, P.; Dhoble, S. J.; Gupta, B. K. Two-dimensional double hydroxide nanoarchitecture with high areal and volumetric capacitance. *ACS Omega* **2018**, *3*, 7204−7213.

(18) Zhang, G.; Qin, P.; Nasser, R.; Li, S.; Chen, P.; Song, J. Synthesis of Co(CO$_3$)$_{0.5}$(OH)/Ni$_2$(CO$_3$)(OH)$_2$ nanobelts and their application in flexible all-solid-state asymmetric supercapacitor. *Chem. Eng. J.* **2020**, *387*, 124029.

(19) Wu, M.; Zheng, W.; Hu, X.; Zhan, F.; He, Q.; Wang, H.; Zhang, Q.; Chen, L. Exploring 2D Energy Storage Materials: Advances in Structure, Synthesis, Optimization Strategies, and Applications for Monovalent and Multivalent Metal-Ion Hybrid Capacitors. *Small* **2022**, *18*, 2205101.

(20) Jing, C.; Dong, B.; Zhang, Y. Chemical modifications of layered double hydroxides in the supercapacitor. *Energy Environ. Mater.* **2020**, *3*, 346−379.

(21) Liu, N.; Lin, J. M.; Wu, J. H.; Huang, M. L.; Fan, L. Q.; Song, Z. Y.; Geng, C. L.; Zhu, T. T.; Pan, W. C. Application of CoV-LDH nanoflower in asymmetric supercapacitors with high electrochemical properties. *Electrochim. Acta* **2020**, *336*, 135550.

(22) Zou, W.; Guo, W.; Liu, X.; Luo, Y.; Ye, Q.; Xu, X.; Wang, F. Anion exchange of Ni−Co layered double hydroxide (LDH) nanoarrays for a high-capacitance supercapacitor electrode: A comparison of alkali anion exchange and sulfuration. *Chem.—Eur. J.* **2018**, *24*, 19309−19316.

(23) Liu, X. X.; Zhou, A. W.; Pan, T.; Dou, Y. B.; Shao, M. F.; Han, J. B.; Wei, M. Ultrahigh-rate-capability of a layered double hydroxide supercapacitor based on a self-generated electrolyte reservoir. *J. Mater. Chem. A* **2016**, *4*, 8421−8427.

(24) Sarigamala, K. K.; Shukla, S.; Struck, A.; Saxena, S. Rationally engineered 3D-dendritic cell-like morphologies of LDH nanostructures using graphene-based core−shell structures. *Microsyst. Nanoeng.* **2019**, *5*, 65.

(25) Wei, M.; Huang, Q. S.; Zhou, Y. P.; Peng, Z.; Chu, W. Ultrathin nanosheets of cobalt-nickel hydroxides hetero-structure via electrodeposition and precursor adjustment with excellent performance for supercapacitor. *J. Energy Chem.* **2018**, *27*, 591−599.

(26) Bai, X.; Liu, J. Y.; Liu, Q.; Chen, R. R.; Jing, X. Y.; Li, B.; Wang, J. In-situ fabrication of MOF-derived Co−Co layered double hydroxide hollow nanocages/graphene composite: A novel electrode material with superior electrochemical performance. *Chem.—Eur. J.* **2017**, *23*, 14839−14847.

(27) Zhou, P.; Wang, C.; Liu, Y.; Wang, Z. Y.; Wang, P.; Qin, X. Y.; Zhang, X. Y.; Dai, Y.; Whangbo, M. H.; Huang, B. B. Sulfuration of NiV-layered double hydroxide towards novel supercapacitor electrode with enhanced performance. *Chem. Eng. J.* **2018**, *351*, 119−126.

(28) Mei, Y.; Zhang, H.; Mei, H.; Kang, W.; Xiao, Z.; Zhang, X.; Fan, W.; Xu, B.; Hu, S. Effective preparation of Ni1.4Co0.6P@C microspheres with prolonged cycling lives for high performance hybrid supercapacitors. *J. Alloys Compd.* **2020**, *818*, 152828.

(29) Li, Q.; Lu, C.; Chen, C.; Xie, L.; Liu, Y.; Li, Y.; Kong, Q.; Wang, H. Layered NiCo$_2$O$_4$/reduced graphene oxide composite as an advanced electrode for supercapacitor. *Energy Storage Mater.* **2017**, *8*, 59−67.

(30) Rama Raju, G. S.; Pavitra, E.; Nagaraju, G.; Sekhar, S. C.; Ghoreishian, S. M.; Kwak, C. H.; Yu, J. S.; Huh, Y. S.; Han, Y. K. Rational design of forest-like nickel sulfide hierarchical architectures

with ultrahigh areal capacity as a binder-free cathode material for hybrid supercapacitors. *J. Mater. Chem. A* **2018**, *6*, 13178−13190.

(31) Xu, X.; Liu, Y.; Dong, P.; Ajayan, P. M.; Shen, J.; Ye, M. Mesostructured $CuCo_2S_4$/$CuCo_2O_4$ nanoflowers as advanced electrodes for asymmetric supercapacitors. *J. Power Sources* **2018**, *400*, 96−103.

(32) Liu, Y.; Wang, Z.; Zhong, Y.; Tade, M.; Zhou, W.; Shao, Z. Molecular design of mesoporous NiCo2O4 and NiCo2S4 with submicrometer-polyhedron architectures for efficient pseudocapacitive energy storage. *Adv. Funct. Mater.* **2017**, *27*, 1701229.

(33) Yu, J.; Gao, X.; Cui, Z.; Jiao, Y.; Zhang, Q.; Dong, H.; Yu, L.; Dong, L. Facile synthesis of binary transition metal sulfide tubes derived from NiCo-MOF-74 for high-performance supercapacitors. *Energy Technol.* **2019**, *7*, 1900018.

(34) Zhao, X.; Mao, L.; Cheng, Q.; Li, J.; Liao, F.; Yang, G.; Xie, L.; Zhao, C.; Chen, L. Two-dimensional Spinel Structured Co-based Materials for High Performance Supercapacitors: A Critical Review. *Chem. Eng. J.* **2020**, *387*, 124081.

(35) Qiao, J.; Zhang, X.; Liu, C.; Zeng, Z.; Yang, Y.; Wu, L.; Wang, F.; Wang, Z.; Liu, W.; Liu, J. Facile synthesis of MnS nanoparticle embedded porous carbon nanocomposite fibers for broadband electromagnetic wave absorption. *Carbon* **2022**, *191*, 525−534.

(36) Wang, X.; Hu, J.; Liu, W.; Wang, G.; An, J.; Lian, J. Ni-Zn binary system hydroxide, oxide and sulfide materials: synthesis and high supercapacitor performance. *J. Mater. Chem. A* **2015**, *3*, 23333−23344.

(37) Zhu, Y. Y.; An, S. L.; Sun, X. J.; Lan, D. W.; Cui, J. L.; Zhang, Y. Q.; He, W. X. Core-branched $NiCo_2S_4$@CoNi-LDH heterostructure as advanced electrode with superior energy storage performance. *Chem. Eng. J.* **2020**, *383*, 123306.

(38) Zhang, R.; Wu, N.; Pan, F.; Yang, Y.; Li, B.; Wu, L.; Liu, W.; Liu, J.; Zeng, Z. Scalable manufacturing of light, multifunctional cellulose nanofiber aerogel sphere with tunable microstructure for microwave absorption. *Carbon* **2023**, *203*, 181−190.

(39) Cheng, S.; Shi, T.; Chen, C.; Zhong, Y.; Huang, Y.; Tao, X.; Li, J.; Liao, G.; Tang, Z. Construction of porous $CuCo_2S_4$ nanorod arrays via anion exchange for high-performance asymmetric supercapacitor. *Sci. Rep.* **2017**, *7*, 6681.

(40) Guo, S. H.; Chen, W. Q.; Li, M.; Wang, J.; Liu, F.; Cheng, J. P. Effect of reaction temperature on the amorphous-crystalline transition of copper cobalt sulfide for supercapacitors. *Electrochim. Acta* **2018**, *271*, 498−506.

(41) Cui, X.; Xiao, P.; Wang, J.; Zhou, M.; Guo, W.; Yang, Y.; He, Y.; Wang, Z.; Yang, Y.; Zhang, Y.; Lin, Z. Highly branched metal alloy networks with superior activities for the methanol oxidation reaction. *Angew. Chem. Int. Ed. Engl.* **2017**, *56*, 4488−4493.

(42) Jadhav, H. S.; Pawar, S. M.; Jadhav, A. H.; Thorat, G. M.; Seo, J. G. Hierarchical mesoporous 3D flower-like $CuCo_2O_4$/NF for high-performance electrochemical energy storage. *Sci. Rep.* **2016**, *6*, 31120.

(43) Samanta, S.; Srivastava, R. $CuCo_2O_4$ based economical electrochemical sensor for the nanomolar detection of hydrazine and metal. *J. Electroanal. Chem.* **2016**, *777*, 48−57.

(44) Lin, J. H.; Jia, H. N.; Liang, H. Y.; Chen, S. L.; Cai, Y. F.; Qi, J.; Qu, C. Q.; Cao, J.; Fei, W. D.; Feng, J. C. Hierarchical $CuCo_2S_4$@NiMn-layered double hydroxide coreshell hybrid arrays as electrodes for supercapacitors. *Chem. Eng. J.* **2018**, *336*, 562−569.

(45) Wu, D.; Ma, W.; Mao, Y.; Deng, J.; Wen, S. Enhanced sulfidation xanthate flotation of malachite using ammonium ions as activator. *Sci. Rep.* **2017**, *7*, 2086.

(46) Li, H.; Li, Z.; Wu, Z.; Sun, M.; Han, S.; Cai, C.; Shen, W.; Liu, X. D.; Fu, Y. Q. Enhanced electrochemical performance of $CuCo_2S_4$/carbon nanotubes composite as electrode material for supercapacitors. *J. Colloid Interface Sci.* **2019**, *549*, 105−113.

(47) Zigan, F.; Joswig, W.; Schuster, H. D.; Mason, S. A. Refinement of the crystal structure of malachite, $Cu_2(OH)_2CO_3$, by neutron diffraction. *Z. Kristallogr.* **1977**, *145*, 412−426.

(48) González-López, J.; Cockcroft, J. K.; Fernández-González, Á.; Jimenez, A.; Grau-Crespo, R. Crystal structure of cobalt hydroxide carbonate $Co_2CO_3(OH)_2$: density functional theory and X-ray diffraction investigation. *Acta Crystallogr., Sect. B: Struct. Sci., Cryst. Eng. Mater.* **2017**, *73*, 868−873.

(49) Shimada, M.; Kanamaru, F.; Koizumi, M.; Yamamoto, N. Preparation of a new Cu-substituted cobaltite spinel: $CuCo_2O_4$. *Mater. Res. Bull.* **1975**, *10*, 733−736.

(50) Riedel, E.; Horvath, E. Kationen-Anionen-Abstände in Kupfer- und Chrom-Thiospinellen. *Mater. Res. Bull.* **1973**, *8*, 973−982.

(51) Chen, S.; Chen, H.; Fan, M.; Li, C.; Shu, K. Sea urchin-like Ni−Co sulfides with different Ni to Co ratios for superior electrochemical performance. *J. Sol-Gel Sci. Technol.* **2016**, *80*, 119−125.

(52) Dong, F.; Guo, Y.; Zhang, D.; Zhu, B.; Huang, W.; Zhang, S. Gold nanoparticles supported on urchin-like CuO: synthesis, characterization, and their catalytic performance for CO oxidation. *Nanomat* **2019**, *10*, 67.

(53) Jia, H.; Cai, Y.; Wang, Z.; Zheng, X.; Li, C.; Liang, H.; Qi, J.; Cao, J.; Feng, J.; Fei, W. Sea urchin-like $CuCo_2S_4$ microspheres with a controllable interior structure as advanced electrode materials for high-performance supercapacitors. *Inorg. Chem. Front.* **2020**, *7*, 603−609.

(54) Gao, Q.; Wang, J.; Wang, J. Morphology-controllable synthesis of $CuCo_2O_4$ arrays on Ni foam as advanced electrodes for supercapacitors. *J. Alloys Compd.* **2019**, *789*, 193−200.

(55) Rafai, S.; Qiao, C.; Naveed, M.; Wang, Z.; Younas, W.; Khalid, S.; Cao, C. Microwave-anion-exchange route to ultrathin cobalt-nickel-sulfide nanosheets for hybrid supercapacitors. *Chem. Eng. J.* **2019**, *362*, 576−587.

(56) Ahmed, A. T. A.; Pawar, S. M.; Inamdar, A. I.; Im, H.; Kim, H. Fabrication of FeO@$CuCo_2S_4$ multifunctional electrode for ultrahigh-capacity supercapacitors and efficient oxygen evolution reaction. *Int. J. Energy Res.* **2019**, *44*, 1798−1811.

(57) Bera, A.; Maitra, A.; Das, A. K.; Halder, L.; Paria, S.; Si, S. K.; De, A.; Ojha, S.; Khatua, B. B. A quasi-solid-state asymmetric supercapacitor device based on honeycomb-like nickel-copper-carbonate-hydroxide as a positive and Iron Oxide as a negative electrode with superior electrochemical performances. *ACS Appl. Electron. Mater.* **2020**, *2*, 177−185.

(58) Sheng, P.; Tao, S.; Gao, X.; Tan, Y.; Wu, D.; Qian, B.; Chu, P. K. Design and synthesis of dendritic Co_3O_4@$Co_2(CO_3)(OH)_2$ nano-arrays on carbon cloth for high-performance supercapacitors. *J. Mater. Sci.* **2020**, *55*, 12091−12102.

(59) George, A.; Kundu, M. Construction of self-supported hierarchical $CuCo_2O_4$ dendrites as faradaic electrode material for redox-based supercapacitor applications. *Electrochim. Acta* **2022**, *433*, 141204.

(60) George, A.; Kundu, M. Copper-cobalt-based sulfides: strategy to boost energy storage performance utilizing the synergistic effect of a double metal ion. *Energy Fuels* **2022**, *36*, 12327−12340.

(61) Yao, M.; Hu, Z.; Liu, Y.; Liu, P.; Ai, Z.; Rudolf, O. 3d hierarchical mesoporous roselike NiO nanosheets for high-performance supercapacitor electrodes. *J. Alloys Compd.* **2015**, *648*, 414−418.

(62) Xia, P.; Wang, Q.; Wang, Y.; Quan, W.; Jiang, D.; Chen, M. Hierarchical $NiCo_2O_4$@Ni$(OH)_2$ core-shell nanoarrays as advanced electrodes for asymmetric supercapacitors with high energy density. *J. Alloys Compd.* **2019**, *771*, 784−792.

(63) Hu, W.; Chen, L.; Du, M.; Song, Y.; Wu, Z.; Zheng, Q. Hierarchical NiCo-layered double hydroxide nanoscroll@PANI nanocomposite for high performance battery-type supercapacitor. *Electrochim. Acta* **2020**, *338*, 135869.

(64) Lv, L.; Xu, K.; Wang, C.; Wan, H.; Ruan, Y.; Liu, J.; Zou, R.; Miao, L.; Ostrikov, K. K.; Lan, Y.; et al. Intercalation of Glucose in NiMn-Layered Double Hydroxide Nanosheets: an Effective Path Way towards Battery-type Electrodes with Enhanced Performance. *Electrochim. Acta* **2016**, *216*, 35−43.

(65) Kundu, M.; Liu, L. Direct growth of mesoporous MnO_2 nanosheet arrays on nickel foam current collectors for high-performance pseudocapacitors. *J. Power Sources* **2013**, *243*, 676−681.

(66) Ghosh, D.; Giri, S.; Das, C. K. Synthesis, characterization and electrochemical performance of graphene decorated with 1D $NiMoO_4$ nH_2O nanorods. *Nanoscale* **2013**, *5*, 10428.

(67) Purkait, T.; Singh, G.; Kumar, D.; Singh, M.; Dey, R. S. High-performance flexible supercapacitors based on electrochemically tailored three-dimensional reduced graphene oxide networks. *Sci. Rep.* **2018**, *8*, 640.

(68) Liu, W.; Niu, H.; Yang, J.; Cheng, K.; Ye, K.; Zhu, K.; Wang, G.; Cao, D.; Yan, J. Ternary transition metal sulfides embedded in graphene nanosheets as both the anode and cathode for high-performance asymmetric supercapacitors. *Chem. Mater.* **2018**, *30*, 1055−1068.

(69) Zhao, T.; Yang, W.; Zhao, X.; Peng, X.; Hu, J.; Tang, C.; Li, T. Facile preparation of reduced graphene oxide/copper sulfide composite as electrode materials for supercapacitors with high energy density. *Composites, Part B* **2018**, *150*, 60−67.

(70) Shah, M. Z. U.; Sajjad, M.; Hou, H.; Rahman, S.; Shah, A. Copper sulfide nanoparticles on titanium dioxide (TiO_2) nanoflakes: A new hybrid asymmetrical faradaic supercapacitors with high energy density and superior lifespan. *J. Energy Storage* **2022**, *55*, 105651.

(71) Yang, H.; Kannappan, S.; Pandian, A. S.; Jang, J. H.; Lee, Y. S.; Lu, W. Graphene supercapacitor with both high power and energy density. *Nanotechnology* **2017**, *28*, 445401.

(72) Wu, X.; Huang, B.; Wang, Q.; Wang, Y. Wide potential and high energy density for an asymmetric aqueous supercapacitor. *J. Mater. Chem. A* **2019**, *7*, 19017−19025.

(73) Ghosh, D.; Giri, S.; Moniruzzaman, M.; Basu, T.; Mandal, M.; Das, C. K. α-MnMoO$_4$/graphene hybrid composite: high energy density supercapacitor electrode material. *Dalton Trans.* **2014**, *43*, 11067−11076.

(74) Li, B.; Dai, F.; Xiao, Q.; Yang, L.; Shen, J.; Zhang, C.; Cai, M. Nitrogen-doped activated carbon for a high energy hybrid super-capacitor. *Energy Environ. Sci.* **2016**, *9*, 102−106.

(75) Xiao, Y.; Su, D.; Wang, X.; Wu, S.; Zhou, L.; Sun, Z.; Wang, Z.; Fang, S.; Li, F. Ultrahigh energy density and stable supercapacitor with 2D NiCoAl Layered double hydroxide. *Electrochim. Acta* **2017**, *253*, 324−332.

(76) Wu, S.; Chen, Y.; Jiao, T.; Zhou, J.; Cheng, J.; Liu, B.; Yang, S.; Zhang, K.; Zhang, W. An aqueous Zn-ion hybrid supercapacitor with high energy density and ultrastability up to 80 000 cycles. *Adv. Energy Mater.* **2019**, *9*, 1902915−1902917.

(77) Li, J.; Wang, N.; Tian, J.; Qian, W.; Chu, W. Cross-coupled macro-mesoporous carbon network toward record high energy-power density supercapacitor at 4 V. *Adv. Funct. Mater.* **2018**, *28*, 1806153−1806159.

(78) Wang, S.; Song, Y.; Ma, Y.; Zhu, Z.; Zhao, C.; Zhao, C. Attaining a high energy density of 106 Wh kg-1 for aqueous supercapacitor based on VS$_4$/rGO/CoS$_2$@Co electrode. *Chem. Eng. J.* **2019**, *365*, 88−98.

(79) Bahaa, A.; Balamurugan, J.; Kim, N. H.; Lee, J. H. Metal−organic framework derived hierarchical copper cobalt sulfide nanosheet arrays for high-performance solid-state asymmetric supercapacitors. *J. Mater. Chem. A* **2019**, *7*, 8620−8632.

(80) Lan, M.; Liu, B.; Zhao, R.; Dong, M.; Wang, X.; Fang, L.; Wang, L. Dandelion-like CuCo$_2$O$_4$ arrays on Ni foam as advanced positive electrode material for high-performance hybrid supercapacitors. *J. Colloid Interface Sci.* **2020**, *566*, 79−89.

(81) Lang, X.; Zhang, H.; Xue, X.; Li, C.; Sun, X.; Liu, Z.; Nan, H.; Hu, X.; Tian, H. Rational design of La$_{0.85}$Sr$_{0.15}$MnO$_3$@NiCo$_2$O$_4$ Core−Shell architecture supported on Ni foam for high performance supercapacitors. *J. Power Sources* **2018**, *402*, 213−220.

(82) Li, Y.; Huang, B.; Zhao, X.; Luo, Z.; Liang, S.; Qin, H.; Chen, L. Zeolitic imidazolate framework-L-assisted synthesis of inorganic and organic anion-intercalated hetero-trimetallic layered double hydroxide sheets as advanced electrode materials for aqueous asymmetric super-capacitor battery. *J. Power Sources* **2022**, *527*, 231149.

(83) Huang, B.; Wang, H.; Liang, S.; Qin, H.; Li, Y.; Luo, Z.; Zhao, C.; Xie, L.; Chen, L. Two-dimensional porous cobalt−nickel tungstate thin sheets for high performance supercapattery. *Energy Storage Mater.* **2020**, *32*, 105−114.

(84) Wang, H.; He, Q.; Zhan, F.; Chen, L. Fe, Co-codoped layered double hydroxide nanosheet arrays derived from zeolitic imidazolate frameworks for high-performance aqueous hybrid supercapacitors and Zn-Ni batteries. *J. Colloid Interface Sci.* **2023**, *630*, 286−296.

(85) Li, Y.; Luo, Z.; Liang, S.; Qin, H.; Zhao, X.; Chen, L.; Wang, H.; Chen, S. Two-dimensional porous zinc cobalt sulfide nanosheet arrays with superior electrochemical performance for supercapatteries. *J. Mater. Sci. Technol.* **2021**, *89*, 199−208.